Effect of pinholes in Nb_4C_3 MXene sheets on its electrochemical behavior in aqueous electrolytes

Zhao, Shuangshuang; Wang, Xuehang; Kurra, Narendra; Gogotsi, Yury; Gao, Yu

DOI
10.1016/j.elecom.2022.107380

Publication date
2022

Document Version
Final published version

Published in
Electrochemistry Communications

Electrochemistry Communications 142 (2022) 107380

Contents lists available at ScienceDirect

Electrochemistry Communications

journal homepage: www.elsevier.com/locate/elecom

Effect of pinholes in Nb_4C_3 MXene sheets on its electrochemical behavior in aqueous electrolytes

Shuangshuang Zhao [a,b,c], Xuehang Wang [b,d], Narendra Kurra [b,e], Yury Gogotsi [b,*], Yu Gao [a,*]

[a] Key Laboratory of Physics and Technology for Advanced Batteries (Ministry of Education), College of Physics, Jilin University, Changchun 130012, PR China
[b] A. J. Drexel Nanomaterials Institute, and Department of Materials Science and Engineering, Drexel University, Philadelphia, PA 19104, United States
[c] College of Materials and New Energy, South China Normal University, Shanwei 516600, PR China
[d] Storage of Electrochemical Energy (SEE), Department of Radiation Science and Technology, Delft University of Technology, Delft 2629 JB, the Netherlands
[e] Department of Chemistry, Indian Institute of Technology Hyderabad, Kandi, 502284 Sangareddy, TelanganaState, India

ARTICLE INFO

Keywords:
Supercapacitor
MXene
Niobium Carbide
Aqueous electrolyte
Porous film

ABSTRACT

Two-dimensional (2D) niobium carbide, $Nb_4C_3T_x$ (T_x: O, OH, and F), a representative member of the 43 MXene structural motif, has shown promising electrochemical performance in acidic electrolytes. The capacitive performance of $Nb_4C_3T_x$ in neutral aqueous electrolytes has been reported as moderate, but little effort has been made to improve it. In this paper, we report a method to introduce nanopores (pinholes) in $Nb_4C_3T_x$ MXene flakes by adjusting the etching time. The pinholes generated during the etching process improve ion diffusion pathways, which are otherwise hindered by the restacking of the 2D flakes. The "holey $Nb_4C_3T_x$" shows a 50 % improved rate capability at charge/discharge time scales of 1–2 s in 1 M Li_2SO_4, Na_2SO_4, and $(NH_4)_2SO_4$ electrolytes. Our strategy of controlling the permeability of $Nb_4C_3T_x$ sheets can potentially be applied to other MXenes, providing guidance for improving the capacitance and rate capability of 2D materials.

1. Introduction

Fast charging energy storage devices find use in portable electronics and electric vehicles. The requirements to these devices include high power density, low cost, easy assembly, large-scale implementation, long cyclic stability, and good safety [1–3]. MXenes, two-dimensional (2D) transition metal carbides and nitrides, have attracted great attention for their use as fast-charging electrochemical energy storage electrodes due to their high metallic conductivity, hydrophilicity and tunable interlayer spacing for ion insertion/deinsertion [4–6]. The general formula of MXene is $M_{n+1}X_nT_x$, where M is a transition metal, X is C and/or N and T_x is surface termination(s) such as OH, O, F, etc. [7–8].

Among the numerous MXene family members, the efforts have been primarily devoted to improving the electrochemical performance of $Ti_3C_2T_x$. Increasing the interlayer space, such as introducing graphene, amorphous carbon, metal oxides, and even water, has been considered as an efficient way to improve MXene's charge storage performance [9–13]. For example, the capacitance of $Ti_3C_2T_x$ "clay" is 245 F/g (1 M H_2SO_4, 2 mV/s) [14], but after expanding the interlayer space by annealing the $Ti_3C_2T_x$ under an ammonia atmosphere, the capacitance reached up to 570 F/g (1 M H_2SO_4, 2 mV/s) [15]. The interlayer spacing of the carbon intercalated sandwiched structure of $Ti_3C_2T_x$/C expanded from 1.00 to 2.83 nm, displayed reversible gravimetric capacitance of 364 F/g (1 M H_2SO_4, 1 A/g) [16]. Highly flexible MnO_x/Ti_3C_2 film fabricated by electrostatic interactions effectively prevented the restacking of Ti_3C_2 sheets, enlarged the interlayer spacing, and exhibited excellent capacitance of 259 F/g (2 mV/s, 1 M Li_2SO_4) [17]. $Ti_3C_2T_x$ hydrogel electrode prepared by intercalation of water demonstrated high capacitance of 375 F/g (3 M H_2SO_4, 2 mV/s) [18]. Replacing the acidic and basic electrolytes with neutral aqueous electrolytes can improve safety and lower corrosion risk for practical application. However, the commonly used neutral electrolytes, such as Li_2SO_4, Na_2SO_4, $(NH_4)_2SO_4$ and $MgSO_4$, usually show low capacitance when employed with MXene-based electrodes because of their large hydrated ionic radius and weak redox reaction with the MXene surface [19]. For example, the specific capacitance of $Ti_3C_2T_x$/CNT paper in 1 M $MgSO_4$, $Ti_3C_2T_x$ in 1 M Li_2SO_4 and $Ti_3C_2T_x$/polypyrrole in 1 M Na_2SO_4 is 150 F/g (2 mV/s) [20], 100 F/g (5 mV/s) [21] and 184 F/g (2 mV/s) [22], respectively, which are all much lower compared to the capacitance values recorded in the acidic electrolyte. Thus, adding spacer is not sufficient to improve the capacitance in the neutral aqueous electrolyte;

* Corresponding authors.
E-mail addresses: gogotsi@drexel.edu (Y. Gogotsi), yugao@jlu.edu.cn (Y. Gao).

https://doi.org/10.1016/j.elecom.2022.107380
Received 1 October 2022; Received in revised form 19 October 2022; Accepted 20 October 2022
Available online 21 October 2022

there is still much room for improvement.

Another way to assist the ion transport and increase the layered material's capacitances is to create a porous architecture. In general, the introduction-removal strategy is applied to prepare porous MXene. Templating can introduce macropores by first mixing poly(methyl methacrylate) (PMMA) or polystyrene (PS) spheres with colloidal solutions of $Ti_3C_2T_x$ and then annealing at 400–450 °C followed by removing the polymer spheres [23–24]. The macroporous $Ti_3C_2T_x$ films show improved gravimetric capacitance and outstanding high-rate performance [18]. Further compression of the macroporous MXene can enhance the volumetric capacitance while maintaining a high rate capability [25]. Besides polymeric templates, researchers also produced a porous and anisotropic $Ti_3C_2T_x$ by sulfur loading-removal [26]. Porous $Ti_3C_2T_x$ was also prepared by introducing a transition metal salt ($CuSO_4$, $CoSO_4$, or $FeSO_4$) followed by the removal of the metal oxide (TiO_2) [27]. Typically, these methods require a second step to remove the template, making the process complicated and expensive.

$Nb_4C_3T_x$, as a representative M_4X_3 MXene, attracted growing attention because of its superior electrical and mechanical properties [28]. In addition, the environmental stability and the interlayer spacing available for ion transport make it a promising electrode material, as shown by its capacitance of 276 F/g obtained in 1 M H_2SO_4 for a freestanding film [29]. However, its modest electronic conductivity compared to $Ti_3C_2T_x$ MXene, and thick MXene lamellas impermeable to ions, limit the performance at high rates. Here, we used a "one-step" method to introduce pinholes into the MXene flakes without any templates or additives to improve the capacitance and rate performance of $Nb_4C_3T_x$ flexible film in neutral aqueous electrolyte. In the etching process, pinholes are introduced into the surface of MXene by adjusting the reaction time, which not only saves the cost, but also minimizes oxidation of the material and results in a high yield.

2. Materials and methods

2.1. Preparation of $Nb_4C_3T_x$ film

Powders of niobium (99.9% metals basis, Aladdin, 325 mesh), aluminum (99.8% purity, Aladdin, 300 mesh), and graphite (99.95% purity, Aladdin, 325 mesh) were used as precursors for the synthesis of Nb_4AlC_3. The synthetic method is the same as previously reported [30]. During the etching step, 0.4 g Nb_4AlC_3 powder was added to 30 mL hydrofluoric acid solution (HF, 51 wt%, Sigma Aldrich) under stirring at room temperature (20–25 °C) for 6 days, 8 days and 10 days, named 6-$Nb_4C_3T_x$, 8-$Nb_4C_3T_x$ and 10-$Nb_4C_3T_x$, respectively. These acidic mixtures were washed by de-ionized water (DI H_2O), followed by centrifugation (3500 rpm, 2 min per cycle). After each centrifugation cycle, the supernatant was discarded and the sediment was dispersed in DI H_2O until neutral pH (~7) was reached. In order to delaminate the $Nb_4C_3T_x$, 1 mL of organic base, tetramethylammonium hydroxide (TMAOH 25% in H_2O, Sigma Aldrich) was mixed with 9 mL DI H_2O added to $Nb_4C_3T_x$ and shook for 15 min. at room temperature. The excess TMAOH was separated from the product by repeated centrifugation at 9000 rpm. The resulting wet sediment formed clay-like paste that could be rolled between water-permeable membranes to produce flexible, freestanding films, with a density of ~ 2.82 g cm^{-3} and ~ 2.74 g cm^{-3}, ~3.01 g cm^{-3} for 6-$Nb_4C_3T_x$, 8-$Nb_4C_3T_x$ and 10-$Nb_4C_3T_x$, respectively. Etching for 10 days led to excessive flake damage, making the material fragile, affecting the stability of the structure and resulting in poor rate capability. Therefore, data for this material are only provided in SI for comparison.

2.2. Material characterization

An X-ray diffractometer (XRD, Miniflex Rigaku, USA) with Cu Kα radiation (λ = 1.5406 Å) was used to characterize $Nb_4C_3T_x$ structure at a step size of 0.02° with 0.5 s dwelling time. The electrical conductivity of the films was tested by a 4-point probe setup (Jandel ResTest). A transmission electron microscope (TEM, JEOL-2100, Japan) was used to image the morphology and microstructure of the samples. Brunauer-Emmett-Teller (BET, Beijing Builder kubo-x1000, China) was carried out to analyse the specific surface area and pore size distribution of 8-$Nb_4C_3T_x$. X-ray photoelectron spectroscopy (XPS) measurements were carried out on a PHI VersaProbe 5000 instrument (Physical Electronics, USA) using monochromatic Al-Kα X-rays (50 W, 1486.6 eV, 200 μm spot size). Charge neutralization was applied using a dual beam setup irradiating low energy Ar^+ ions and electrons. Survey spectra were collected using a pass energy of 117.4 eV and energy resolution of 0.5 eV and the core level region spectra were collected using a pass energy of 23.5 eV and energy resolution of 0.05 eV. Quantification and peak fitting were conducted using CasaXPS (V2.3.19). Binding energy scale correction was applied using the adventitious carbon C—C peak at 284.8 eV. Mixed Gaussian-Lorentzian models were used for oxygen containing species (e.g. Nb-O) and asymmetric Lorentzian models were used for metal containing species (e.g. Nb-C). The Shirley model [31] was used for background fitting.

2.3. Preparation of electrode and electrochemical measurements

The electrochemical performance was investigated using three-electrode Swagelok cells. The delaminated $Nb_4C_3T_x$ film was the working electrode, overcapacitive activated carbon was the counter electrode, a cellulose membrane was the separator, and Ag/AgCl was used as the reference electrode. 1 M Li_2SO_4, 1 M Na_2SO_4, and 1 M $(NH_4)_2SO_4$ solutions were used as electrolytes. The electrochemical performance was investigated at room temperature using a VMP3 electrochemical workstation (BioLogic, France), to perform cyclic voltammetry (CV), galvanostatic charge–discharge (GCD) and electrochemical impedance spectroscopy (EIS) measurements. EIS was performed in the frequency range from 10 mHz to 200 kHz.

2.4. Electrochemical calculations

Gravimetric specific capacitance (C_g) was calculated through the following equation:

$$C_g = \frac{1}{\Delta V m v}\int i dV \quad (1)$$

where i is the current, V is the potential window, v is the potential scan rate, and m is the mass of the electrode. The volumetric capacitance (C_V) was calculated according to the following equation:

$$C_V = \rho C_g \quad (2)$$

where ρ is the density of the film.

3. Results and discussion

3.1. Structural characterization

In recent years, the typical MXene material, $Ti_3C_2T_x$, has been widely studied, and its preparation methods have been improved from the initial etching in concentrated HF [32] to a mixture of HCl and LiF (MILD method) [33], HCl and HF [34], or Lewis acid molten salts as etchants [35–36]. However, for $Nb_4C_3T_x$ and other 43 MAX phases, only HF is used for etching because of its thicker monolayers (4 layers of transition metal and 3 layers of carbon). Here, HF (51 wt%) was also selected as the etching reagent, and TMAOH was used as the delamination agent. The detailed procedures for etching and delamination are discussed in the experimental section. Fig. 1 shows the structural aspects of 6-$Nb_4C_3T_x$ and 8-$Nb_4C_3T_x$ films. By comparing the XRD (Fig. 1a and Figure S1) patterns of the two samples, it can be seen that the MAX phase is completely etched. By looking at the amplified portion at (0 0 2) peak,

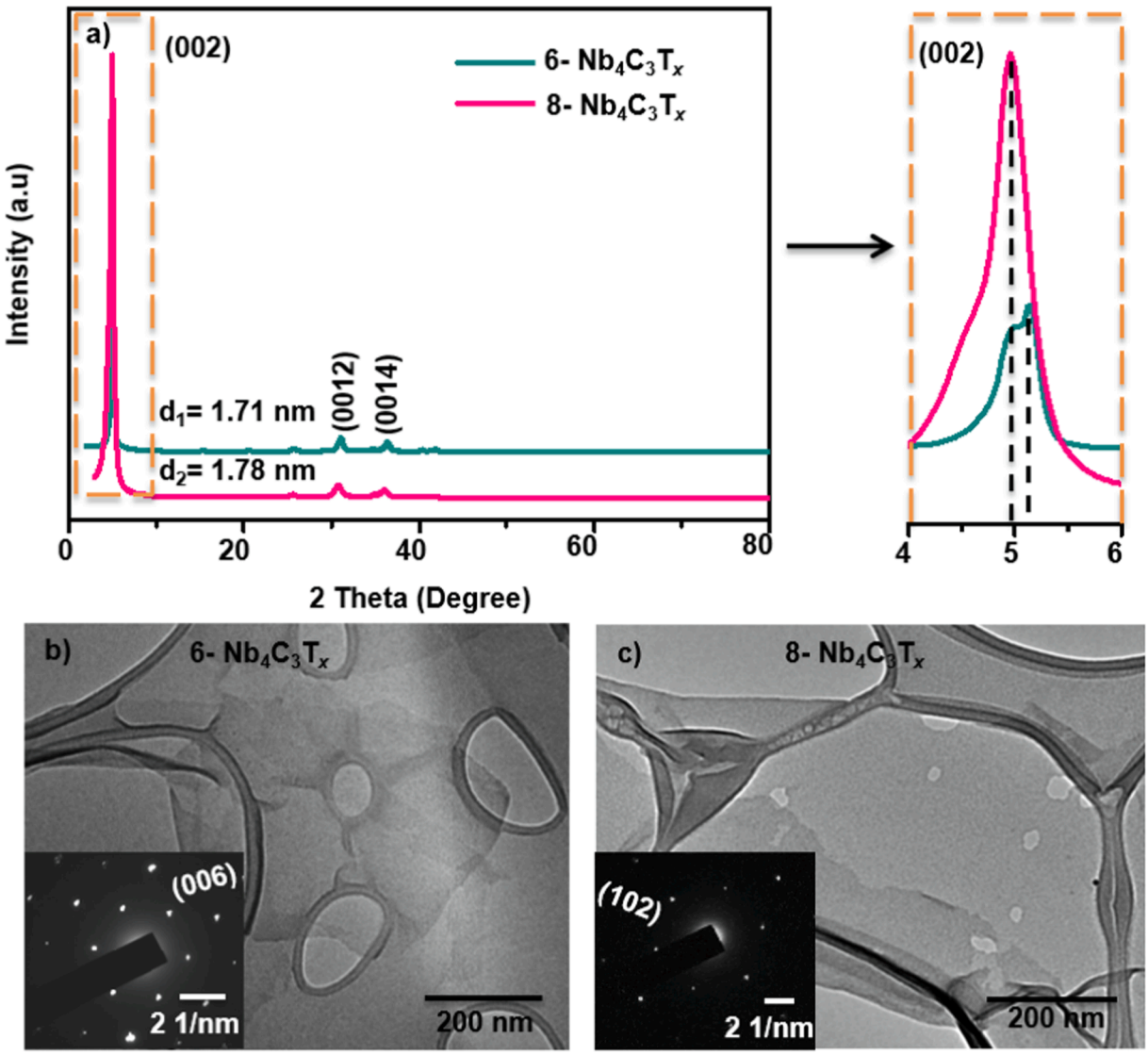

Fig. 1. (a) XRD patterns of $Nb_4C_3T_x$ films. TEM images of (b) 6-$Nb_4C_3T_x$ and (c) 8-$Nb_4C_3T_x$ flakes. Inset shows SAED patterns of respective crystalline single-layer flakes.

the position of the 8-$Nb_4C_3T_x$ shifted to a lower angle (from 5.16° to 4.96°), indicating an enlargement of interlayer space. According to Bragg's equation, the *d*-spacing of 6-$Nb_4C_3T_x$ and 8-$Nb_4C_3T_x$ are 1.71 nm and 1.78 nm, respectively. Transmission electron microscopy (TEM) results (Fig. 1b-c) showed that both samples exhibited transparent lamellar structures, and selective area electron diffraction (SAED) clearly shows the typical hexagonal structure, indicating the etching and delamination processes were successful. Compared to the smooth surface of the 6-$Nb_4C_3T_x$, there are some irregular pinholes in the 8-$Nb_4C_3T_x$. According to the Brunauer-Emmett-Teller (BET) method, 8-$Nb_4C_3T_x$ showed a pore size distribution in the range from 2 to 65 nm, as shown in Figure S2. Moreover, the electrical conductivity of the two samples also showed a significant difference: the conductivity of the 8-$Nb_4C_3T_x$ is about 3. 1 ± 0.1 × 10^3 S/m, which is about half of the 6-$Nb_4C_3T_x$ (5.9 ± 0.1 × 10^3 S/m).

XPS analysis was carried out further to explore the surface chemistry of the two samples, as shown in Fig. 2. The high-resolution XPS spectrum in the O 1*s* region (Fig. 2a) could be fit by 3 peaks at binding energies 529.75 eV, 531 eV and 532.48 eV, which indicate different components and concentrations, Nb-O (39.42% of O 1*s* photoemission), Nb-OH (53.56% of O 1*s* photoemission) and H_2O (7.02% of O 1*s* photoemission), respectively [37–38]. Similar results appear in the spectrum of O 1*s* in the sample of 8-$Nb_4C_3T_x$. But the difference is that the concentration of H_2O (26.66% of O 1*s* photoemission) has increased. It could be attributed to a more complete etching process resulting in a larger interlayer space, allowing more water molecules to enter. According to previous literature, MXenes with larger interspaces and a greater amount of interlayer water can improve the capacitance, as well as the cyclic stability [39]. The spectrum in the C 1*s* region of both samples (Fig. 2b and Fig. 2e) could be fit by four peaks at the position about 282.22 eV, 284.79 eV, 286.02 eV and 287.89 eV, corresponding to the bands of Nb-C, C—C, C—O, C═O, respectively [40]. Moreover, the Nb spectrum also confirms the presence of oxygen-containing functional groups and a small amount of F terminations. The detailed composition, peak position, and concentration are shown in **Table S1**. In addition, Figure S3 clearly shows a weak peak at 400.98 eV in XPS full spectrum of both samples, it is attributed to R-NH_3^+, indicating that there is some TMA^+ intercalated between MXene sheets. It enlarges the interlayer spacing and further facilitates the diffusion of electrolyte ions across MXene galleries, but the intercalated TMA^+ cation is not expected to contribute to charge storage [29,38].

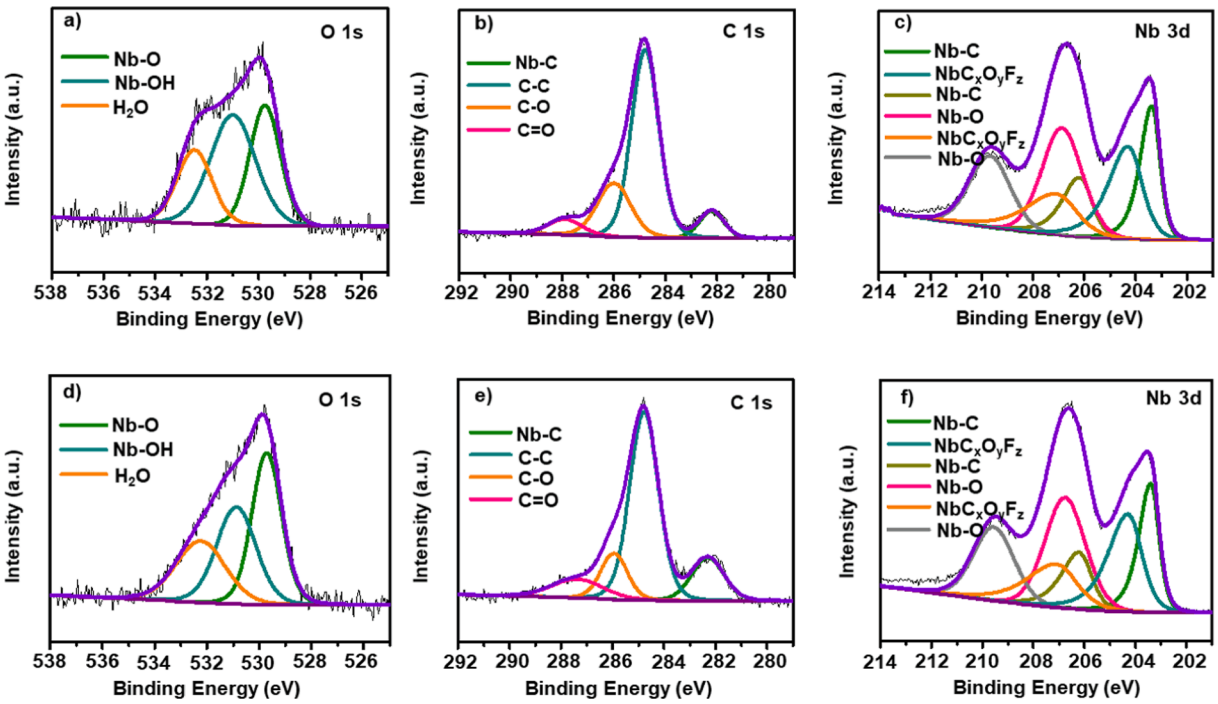

Fig. 2. XPS core level spectra of (a-c) 6-$Nb_4C_3T_x$ and (d-f) 8-$Nb_4C_3T_x$ MXene films. (a, d) O 1*s*; (b, e) C 1*s* and (c, f) Nb 3*d* regions. Peak fitting was done to deconvolute the various components as assigned in the respective spectrum.

3.2. *Electrochemical characterization*

The electrochemical performance of the two different $Nb_4C_3T_x$ flexible films was conducted by three-electrode system in the potential window of −0.8 to 0 V *vs* Ag/AgCl in 1 M Li_2SO_4, as shown in Fig. 3. By comparing the cyclic voltammetry (CV) curves of the two samples at different scan rates, a pair of wide redox peaks appeared, with cathodic peak at about −0.64 V (*vs* Ag/AgCl) and anodic peak around −0.55 V (*vs* Ag/AgCl), indicating that there is contribution from pseudocapacitance [41–42]. In addition, the pH of 1 M Li_2SO_4 is about 8.1[43]; therefore, the redox peaks should be mainly due to the reversible intercalation/deintercalation of Li-ions, instead of protons. Fig. 3c summarizes the gravimetric capacitance of both 6-$Nb_4C_3T_x$ and 8-$Nb_4C_3T_x$ films at different scan rates calculated according to CV curves. At the scan rate of

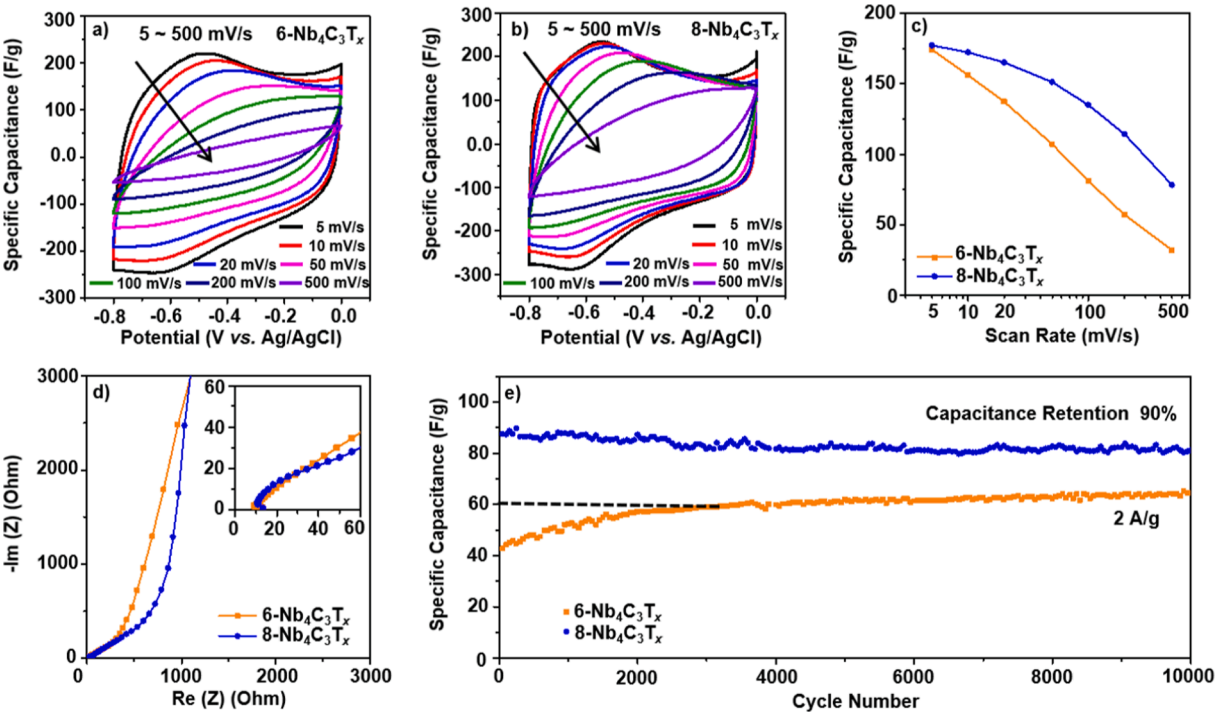

Fig. 3. Electrochemical performance of $Nb_4C_3T_x$ films in 1 M Li_2SO_4 electrolyte. Cyclic voltammograms (CVs) of (a) 6-$Nb_4C_3T_x$ and (b) 8-$Nb_4C_3T_x$ at scan rates from 5 to 500 mV/s in 1 M Li_2SO_4. (c) Variation of specific capacitance versus scan rate. (d) EIS spectra of $Nb_4C_3T_x$ MXene films; inset shows high frequency region of the EIS data. (e) Cycling test was performed by running continuous galvanostatic charge/discharge cycles at 2 A/g for 10,000 cycles.

5 mV/s, the capacitance of 6-$Nb_4C_3T_x$ is about 174 F/g (490 F/cm^3), and for 8-$Nb_4C_3T_x$ is about 177 F/g (485 F/cm^3). Nevertheless, when increasing the scan rate to 500 mV/s, the capacitance of 8-$Nb_4C_3T_x$ is about 78 F/g (214 F/cm^3), almost 2.4 times of the 6-$Nb_4C_3T_x$ (32 F/g, 90 F/cm^3). The corresponding volumetric capacitance at different scan rates is shown in Figure S4. The EIS data in Fig. 3d is used to analyze the dynamic performance of ions in the electrode, which is usually composed of three parts, solution resistance (R_s), charge transfer resistance (R_{ct}), and diffusion of ions within the electrode material [44]. Comparison of the Nyquist plots of two MXene films showed that the 8-$Nb_4C_3T_x$ electrode shows capacitive behavior. Comparing Fig. 3d with the improved specific capacitance at different scan rates (Fig. 3c), the enhanced electrochemical performance may be attributed to the the presence of pinholes, which favor ion access to the electrode and shorten the ion transport path [5,45]. Moreover, the MXene 8-$Nb_4C_3T_x$ with pinholes also possessed excellent cycling stability, as shown in Fig. 3e. At the current density of 2 A/g, its initial capacitance is about 90 F/g, and after 10,000 charges/discharges cycles, the capacitance is about 81 F/g with capacitance retention of 90%. The corresponding charge–discharge curves are shown in Figure S5. Notably, the capacitance of 6-$Nb_4C_3T_x$ increased with cycling number and stabilized at about 3000 cycles, which is similar to its performance in lithium-ion batteries in the previous reports [30]. The increased capacitance with cycling could be due to the increased interlayer spacing from the intercalation/deintercalation of Li-ions.

Different from Li_2SO_4, when 1 M Na_2SO_4 was used as the electrolyte, the CV curve was almost rectangular with no obvious redox peaks (Fig. 4**a-b**), indicating less contribution from the pseudocapacitive process and highly capacitive behaviour [46]. The corresponding gravimetric and volumetric capacitances at different scan rates are shown in Fig. 4c and Figure S6, respectively. At the scan rates of 5 mV/s, 100 mV/s, 500 mV/s, the gravimetric capacitances values of the 6-$Nb_4C_3T_x$ are about 113 F/g (318 F/cm^3), 41 F/g (115 F/cm^3) and 15 F/g (42 F/cm^3). The capacitance retention is about 13.3% (from 5 mV/s to 500 mV/s). But for the 8-$Nb_4C_3T_x$ electrode, at the same scan rate of 5 mV/s, 100 mV/s, and 500 mV/s, the gravimetric capacitance values are about 111 F/g (304 F/cm^3), 89 F/g (243 F/cm^3) and 63 F/g (173 F/cm^3), respectively; and the capacitance retention is about 56.8%, which is almost 4.3 times that of 6-$Nb_4C_3T_x$. Since the pH of 1 M Na_2SO_4 is about 6.4, the main capacitance comes from the capacitive behavior rather than the intercalation of protons in the aqueous solution. The electrochemical impedance spectra of 6- and 8-$Nb_4C_3T_x$ in 1 M Na_2SO_4 are shown in Fig. 4d. At high frequencies, 8-$Nb_4C_3T_x$ exhibits a lower resistance (intercept of semicircle on the real impedance axis). In order to further investigate the diffusion and transport of Na^+ ions in both electrodes, we plotted the linear fit of Z_{real} versus $\omega^{-1/2}$ as shown in Fig. 4e in the low-frequency region according to the relationship:

$$D_{Na^+} = \frac{0.5R^2T^2}{S^2n^4F^4C^2\sigma^2} \tag{3}$$

$$Z_{real} = R_s + R_{ct} + \sigma\omega^{-1/2} \tag{4}$$

where D_{Na+} is diffusion coefficient of sodium ion, R is the gas constant, T is the absolute temperature, S is the surface area of the electrode, n is the number of electrons, F is the Faraday constant and σ is the Warburg factor [47]. In Fig. 4e, the 8-$Nb_4C_3T_x$ electrode presents a lower slope than 6-$Nb_4C_3T_x$ electrodes, demonstrating the faster ion diffusion/transportation kinetics. It agrees with the better rate capability of 8-$Nb_4C_3T_x$ compared to the 6-$Nb_4C_3T_x$ electrode. Combined with the aforementioned analysis results, we drew a simple schematic about the interface of the electrode and electrolyte, as shown in Fig. 4f. In MXene materials without pinholes (6-$Nb_4C_3T_x$), ions in the electrolyte are mainly transmitted through gaps between 2D layers, and the transmission path is long. However, for 8-$Nb_4C_3T_x$ containing pinholes, ions can not only move through the gaps between layers, but also reach the interior of the material more quickly through the pores (pinholes) in MXene sheets. In this way, the ion transport path is effectively shortened to improve the electrochemical performance, especially at a high scan

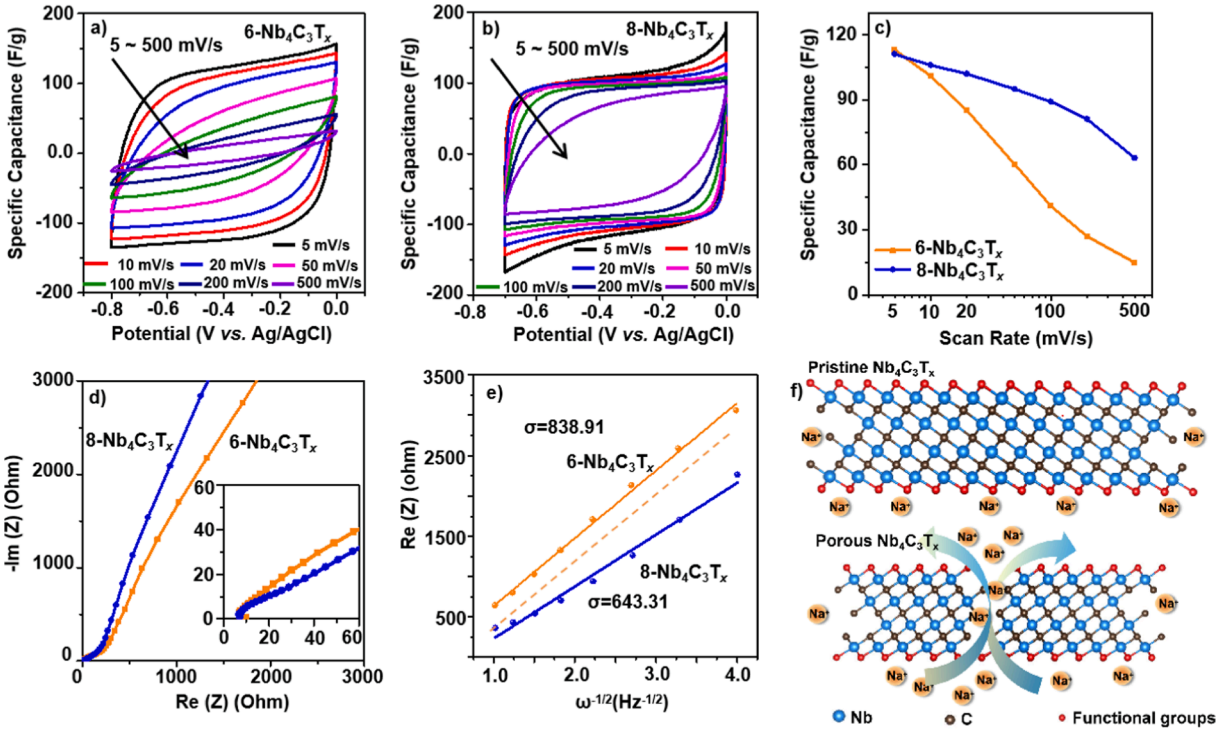

Fig. 4. Electrochemical performance of $Nb_4C_3T_x$ films in 1 M Na_2SO_4 electrolyte. Cyclic voltammograms (CVs) of (a) 6-$Nb_4C_3T_x$ and (b) 8-$Nb_4C_3T_x$ at scan rates from 5 to 500 mV/s in 1 M Na_2SO_4 and (c) corresponding specific capacitance as a function of scan rate. (d) Nyquist plots of $Nb_4C_3T_x$ MXene films, inset shows the high-frequency region of the spectra. (e) Linear fit showing the relationship between Real (Z) and $\omega^{-1/2}$ in the low-frequency region. (f) Schematic illustrating transport of electrolyte ions through $Nb_4C_3T_x$ layers and ion diffusion pathways between MXene sheets and across a $Nb_4C_3T_x$ flake with a pinhole.

rates.

The capacitance of the two materials in 1 M $(NH_4)_2SO_4$ is not satisfactory (Figure S7), although maybe some of the contribution comes from protons in an aqueous solution because the pH of 1 M $(NH_4)_2SO_4$ is about 5.5. The CV curves (Figure S7a and S7b) of both, 6-$Nb_4C_3T_x$ and 8-$Nb_4C_3T_x$, are rectangular and do not have obvious redox peaks. Although 8-$Nb_4C_3T_x$ showed a smaller solution resistances and better ion diffusion in the impedance spectra (the steepest slope of the Nyquist plot in the low-frequency range) (Figure S7d), there was little improvement in capacitance. According to previous literature, the capacitance of MXene in $(NH_4)_2SO_4$ electrolyte is mainly from the electrical double layer formed by the adsorbed NH_4^+ on the surface. Because of the larger hydration ion radius of NH_4^+, more deep-adsorption sites are needed to improve the capacitance [48], and the same conclusion is supported by Figure S8. We further extended the reaction time of Nb_4AlC_3 in HF solution to 10 days and named it 10-$Nb_4C_3T_x$. The calculated interlayer-spacing from XRD data (Figure S8a) was 1.77 nm, between the values of 6-$Nb_4C_3T_x$ and 8-$Nb_4C_3T_x$, which may be due to overetching. However, the electrical conductivity of 10-$Nb_4C_3T_{xwas}$ about $3.0 \pm 0.1 \times 10^3$ S/m, which is almost the same as the conductivity of 8-$Nb_4C_3T_x$. TEM analysis (Figure S8b) shows that, due to excessive etching, not only pinholes but also cracks appear on the surface of the material, which lead to a partial collapse of the material structure. The electrochemical properties of 10-$Nb_4C_3T_x$ in three electrolytes were tested. As expected, the redox peaks of 10-$Nb_4C_3T_x$ only appeared in the CV curve of 1 M Li_2SO_4, with the cathodic peak at about −0.70 V (*vs* Ag/AgCl) and the anodic peak around −0.49 V (*vs* Ag/AgCl). The CV curves in 1 M Na_2SO_4 and 1 M $(NH_4)_2SO_4$ electrolytes showed rectangular box-like profiles. The capacitance was calculated using CV curves and plotted as a function of rate in Figure S8f. At the scan rate of 5 mV/s, the capacitance of 10-$Nb_4C_3T_x$ in 1 M Li_2SO_4, 1 M Na_2SO_4, and 1 M $(NH_4)_2SO_4$ was 191 F/g (575 F/cm^3), 144 F/g (434 F/cm^3) and 136 F/g (410 F/cm^3), respectively, which is better than 6-$Nb_4C_3T_x$ and 8-$Nb_4C_3T_x$ due to the greater amount of pinholes and cracks on the surface. However, the rate performance (around 23% at 500 mV/s relative to 5 mV/s) is poor in this case. Moreover, the resulting overetching and crack formation make the material fragile, affecting the stability of the structure and resulting in poor rate capability.

4. Conclusions

We report on preparation and electrochemical properties of holey $Nb_4C_3T_x$ MXene films manufactured by adjusting etching time during MXene synthesis. The extended HF etching time of eight days introduces pinholes in the 2D MXene sheets, promoting ion diffusion by decreasing the transmission path. The holey MXene shows improved capacitance in Li^+/Na^+ ion aqueous capacitors. The capasitance values of 177 F/g and 111 F/g were obtained in 1 M Li_2SO_4 and 1 M Na_2SO_4 electrolytes at 5 mV/s, respectively. Those electrodes maintained 78 F/g and 63 F/g at the scan rate of 500 mV/s, which were 2.4 and 4.2 times of the pinholes-free $Nb_4C_3T_x$ films, respectively. However, excessive etching for 10 days weakens the mechanical properties of the material. Although $Nb_4C_3T_x$ is just one of many MXenes, this approach may be applicable to other MXenes from 21, 32 and 43 families. It is also not limited to the use of MXenes as electrodes in neutral aqueous electrolytes and can be effective for improving transport in MXene membranes used for filtration, energy storage and conversion and other applications.

CRediT authorship contribution statement

Shuangshuang Zhao: Conceptualization, Methodology, Validation, Investigation, Writing – original draft, Writing – review & editing, Visualization. **Xuehang Wang:** Methodology, Investigation, Writing – review & editing. **Narendra Kurra:** Methodology, Investigation, Writing – review & editing. **Yury Gogotsi:** Conceptualization, Resources, Writing – review & editing, Visualization, Supervision, Project administration, Funding acquisition. **Yu Gao:** Writing – review & editing, Supervision.

Declaration of Competing Interest

The authors declare the following financial interests/personal relationships which may be considered as potential competing interests.

Data availability

Data will be made available on request.

Acknowledgements

The work was conducted at Drexel University and supported by the Fluid Interface Reactions, Structures, and Transport (FIRST) Center, an Energy Frontier Research Center (EFRC) funded by the U.S. Department of Energy, Office of Science, and Office of Basic Energy Sciences. Shuangshuang Zhao was sponsored by China Scholarship Council (CSC). We thank Dr. Christine Hatter, Mark Anayee and Marley Downes for their help with performing TEM analysis, XPS investigations and manuscript revision, respectively.

Author contributions

S S Z and Yury G conceived the project. S S Z fabricated the samples and performed all electrochemical experiments and data analysis with support from X H W and N K. Yury G and Yu G supervised the work and were involved in the evaluation and interpretation of the results. All authors participated in the scientific discussion and contributed to revision of the manuscript written by S S Z.

Appendix A. Supplementary material

Supplementary data to this article can be found online at https://doi.org/10.1016/j.elecom.2022.107380.

References

[1] P. Simon, Y. Gogotsi, Perspectives for electrochemical capacitors and related devices, Nat. Mater 19 (2020) 1151–1163, https://doi.org/10.1038/s41563-020-0747-z.
[2] X.H. Wang, M. Salari, D. Jiang, J.C. Varela, B. Anasori, D.J. Wesolowski, S. Dai, M. W. Grinstaff, Y. Gogotsi, Electrode material–ionic liquid coupling for electrochemical energy storage, Nat Rev Mater 5 (2020) 787–808, https://doi.org/10.1038/s41578-020-0218-9.
[3] C.F. Liu, Y.C. Liu, T.Y. Yi, C.C. Hu, Carbon materials for high-voltage supercapacitors, Carbon 145 (2019) 529–548, https://doi.org/10.1016/j.carbon.2018.12.009.
[4] A. Vahidmohammadi, J. Rosen, Y. Gogotsi, The world of two-dimensional carbides and nitrides (MXenes), Science 372 (2021) 6547, https://doi.org/10.1126/science.abf1581.
[5] K. Li, M.Y. Liang, H. Wang, X.H. Wang, Y.S. Huang, J. Coelho, S. Pinilla, Y. L. Zhang, F.W. Qi, V. Nicolosi, Y.X. Xu, 3D Architectures: 3D MXene Architectures for Efficient Energy Storage and Conversion, Adv. Funct. Mater (2020) 2000842, https://doi.org/10.1002/adfm.202070306.
[6] M. Naguib, M.W. Barsoum, Y. Gogotsi, Ten Years of Progress in the Synthesis and Development of MXenes, Adv. Mater 33 (2021) 2103393, https://doi.org/10.1002/adma.202170303.
[7] M.K. Aslam, Y.B. Niu, M.W. Xu, MXenes for Non-Lithium-Ion (Na, K, Ca, Mg, and Al) Batteries and Supercapacitors, Adv. Energy. Mater 11 (2021) 2000681, https://doi.org/10.1002/aenm.202000681.
[8] A. Saha, N. Shpigel, N. Rosy, S. Leifer, T. Taragin, H. Sharabani, I. Aviv, G. D. Perelshtein, M. Nessim, Y.G. Noked, Enhancing the Energy Storage Capabilities of $Ti_3C_2T_x$ MXene Electrodes by Atomic Surface Reduction, Adv. Funct. Mater 31 (2021) 2106294, https://doi.org/10.1002/adfm.202106294.
[9] J. Li, X.T. Yuan, C. Lin, Y.Q. Yang, L. Xu, X. Du, J.L. Xie, J.H. Lin, J.L. Sun, Achieving High Pseudocapacitance of 2D Titanium Carbide (MXene) by Cation Intercalation and Surface Modification, Adv. Energy. Mater 7 (2017) 1602725, https://doi.org/10.1002/aenm.201602725.
[10] T.Z. Zhou, C. Wu, Y.L. Wang, A.P. Tomsia, M.Z. Li, E. Saiz, S.L. Fang, R. H. Baughman, L. Jiang, Q.F. Cheng, Super-tough MXene-functionalized graphene sheets, Nat. Commun 11 (2021) 2077, https://doi.org/10.1038/s41467-020-15991-6.

[11] Y. Dall'Agnese, P. Rozier, P. L. Taberna, Y. Gogotsi, P. Simon, Capacitance of two-dimensional titanium carbide (MXene) and MXene/carbon nanotube composites in organic electrolytes, J. Power. Sources, 306 (2016), pp. 510-515, 10.1016/j.jpowsour.2015.12.036.

[12] R.B. Rakhi, B. Ahmed, D. Anjum, H.N. Alshareef, Direct Chemical Synthesis of MnO_2 Nanowhiskers on Transition-Metal Carbide Surfaces for Supercapacitor Applications, ACS Appl. Mater. Interfaces 8 (2016) 18806–18814, https://doi.org/10.1021/acsami.6b04481.

[13] X.B. Hui, X.L. Ge, R.Z. Zhao, Z.Q. Li, L.W. Yin, Interface Chemistry on MXene-Based Materials for Enhanced Energy Storage and Conversion Performance, Adv. Funct. Mater 30 (2020) 2005190, https://doi.org/10.1002/adfm.202005190.

[14] M. Ghidiu, M.R. Lukatskaya, M.Q. Zhao, Y. Gogotsi, M.W. Barsoum, Conductive two-dimensional titanium carbide 'clay' with high volumetric capacitance, Nature 516 (2014) 78–81, https://doi.org/10.1038/nature13970.

[15] M. Hu, R. Cheng, Z.J. Li, T. Hu, H. Zhang, C. Shi, J.X. Yang, C. Cui, C. Zhang, H. L. Wang, B.B. Fan, X.H. Wang, Q.H. Yang, Interlayer engineering of $Ti_3C_2T_x$ MXenes towards high capacitance supercapacitors, Nanoscale 12 (2020) 763–771, https://doi.org/10.1039/C9NR08960H.

[16] L. Shen, X. Zhou, X. Zhang, Y. Zhang, Y. Liu, W. Wang, W. Si, X. Dong, Carbon-intercalated $Ti_3C_2T_x$ MXene for high-performance electrochemical energy storage, J. Mater. Chem. A 6 (46) (2018) 23513–23520.

[17] Y.P. Tian, C.H. Yang, W.X. Que, X.B. Liu, X.T. Yin, L.B. Kong, Flexible and free-standing 2D titanium carbide film decorated with manganese oxide nanoparticles as a high volumetric capacity electrode for supercapacitor, J. Power. Sources 359 (2017) 332–339, https://doi.org/10.1016/j.jpowsour.2017.05.081.

[18] M.R. Lukatskaya, S. Kota, Z.F. Lin, M.Q. Zhao, N. Shpige, M.D. Levi, J. Halim, P. L. Taberna, M. W.Barsoum, P. Simon, Y. Gogotsi, Ultra-high-rate pseudocapacitive energy storage in two-dimensional transition metal carbides, Nat. Energy 2 (2017) 17105, https://doi.org/10.1038/nenergy.2017.105.

[19] S. Li, Q. Shi, Y. Li, J. Yang, T.H. Chang, J.W. Jiang, P.Y. Chen, Intercalation of Metal Ions into $Ti_3C_2T_x$ MXene Electrodes for High-Areal-Capacitance Microsupercapacitors with Neutral Multivalent Electrolytes, Adv. Funct. Mater (2020) 2003721, https://doi.org/10.1002/adfm.202003721.

[20] M.Q. Zhao, C.E. Ren, Z. Ling, M.R. Lukatskaya, C.F. Zhang, K.L.V. Aken, M. W. Barsoum, Y. Gogotsi, Flexible MXene/Carbon Nanotube Composite Paper with High Volumetric Capacitance, Adv. Mater 27 (2014) 339–345, https://doi.org/10.1002/adma.201404140.

[21] J. Tang, T.S. Mathis, N. Kurra, A. Sarycheva, X. Xiao, M.N. Hedhili, Q. Jiang, H. N. Alshareef, B.M. Xu, F. Pan, Y. Gogotsi, Tuning the Electrochemical Performance of Titanium Carbide MXene by Controllable in situ Anodic Oxidatio, Angew. Chem. Int. Ed 58 (2019) 17849–17855, https://doi.org/10.1002/anie.201911604.

[22] W.L. Wu, D. Wei, J.F. Zhu, D.J. Niu, F. Wang, L. Wang, L.Q. Yang, P.P. Yang, C. W. Wang, Enhanced electrochemical performances of organ-like Ti_3C_2 MXenes/polypyrrole composites as supercapacitors electrode materials, Ceram. Int 45 (2019) 7328–7337, https://doi.org/10.1016/j.ceramint.2019.01.016.

[23] M.Q. Zhao, X.Q. Xie, C.E. Ren, T. Makaryan, B. Anasori, G.X. Wang, Y. Gogotsi, Hollow MXene Spheres and 3D Macroporous MXene Frameworks for Na-Ion Storage, Adv. Mater 29 (2017), 1702410, https://doi.org/10.1002/adma.201702410.

[24] K. Li, X.H. Wang, S. Li, P. Urbankowski, J.M. Li, Y.X. Xu, Y. Gogotsi, An Ultrafast Conducting Polymer@MXene Positive Electrode with High Volumetric Capacitance for Advanced Asymmetric Supercapacitors, Small 16 (2020) 1906851, https://doi.org/10.1002/smll.201906851.

[25] K. Li, X.H. Wang, X.F. Wang, M.Y. Liang, V. Nicolosi, Y.X. Xu, Y. Gogotsi, All-pseudocapacitive asymmetric MXene-carbon-conducting polymer supercapacitors, Nano. Energy 75 (2020), 104971, https://doi.org/10.1016/j.nanoen.2020.104971.

[26] X.Q. Xie, K. Kretschmer, B. Anasori, B. Sun, G.X. Wang, Y. Gogotsi, Porous $Ti_3C_2T_x$ MXene for Ultrahigh-Rate Sodium-Ion Storage with Long Cycle Life, ACS Appl. Nano Mater 1 (2018) 505–511, https://doi.org/10.1021/acsanm.8b00045.

[27] C.E. Ren, M.Q. Zhao, T. Makaryan, J. Halim, M. Boota, S. Kota, B. Anasori, M. W. Barsoum, Y. Gogotsi, Porous Two-Dimensional Transition Metal Carbide (MXene) Flakes for High-Performance Li-Ion Storage, ChemElectroChem 3 (2016) 689–693, https://doi.org/10.1002/celc.201600059.

[28] A. Lipatov, M. Alhabeb, H. D. Lu, S. S. Zhao, M. J. Loes, N. S. Vorobeva, Y. Dall'Agnese, Y. Gao, A. Gruverman, Y. Gogotsi, A. Sinitskii, Electrical and Elastic Properties of Individual Single-Layer $Nb_4C_3T_x$ MXene Flakes, Adv. Electron. Mater, 6 (2020), p. 1901382, 10.1002/aelm.201901382.

[29] S.S. Zhao, C.F. Chen, X. Zhao, X.F. Chu, F. Du, G. Chen, Y. Gogotsi, Y. Gao, Y. Dall'Agnese, Flexible $Nb_4C_3T_x$ Film with Large Interlayer Spacing for High-Performance Supercapacitors, Adv. Funct. Mater 30 (2020) 2000815, https://doi.org/10.1002/adfm.202000815.

[30] S.S. Zhao, X. Meng, K. Zhu, F. Du, G. Chen, Y.J. Wei, Y. Gogotsi, Y. Gao, Li-ion uptake and increase in interlayer spacing of Nb_4C_3 MXene, Energy. Stor. Mater 8 (2017) 42–46, https://doi.org/10.1016/j.ensm.2017.03.012.

[31] J.E. Castle, A.M. Salvi, Interpretation of the Shirley background in x-ray photoelectron spectroscopy analysis, J. Vac. Sci. Technol. A 19 (2001) 1170–1175, https://doi.org/10.1116/1.1378074.

[32] O. Mashtalir, M. Naguib, B. Dyatkin, Y. Gogotsi, M.W. Barsoum, Kinetics of aluminum extraction from Ti_3AlC_2 in hydrofluoric acid, Mater. Chem. Phys 139 (2013) 147–152, https://doi.org/10.1016/j.matchemphys.2013.01.008.

[33] A. Lipatov, M. Alhabeb, M.R. Lukatskaya, A. Boson, Y. Gogotsi, A. Sinitskii, Effect of Synthesis on Quality, Electronic Properties and Environmental Stability of Individual Monolayer Ti_3C_2 MXene Flakes, Adv. Electron. Mater 2 (2016) 1600255, https://doi.org/10.1002/aelm.201600255.

[34] T.S. Mathis, K. Maleski, A. Goad, A. Sarycheva, M. Anayee, A.C. Foucher, K. Hantanasirisakul, C.E. Shuck, E.A. Stach, Y. Gogotsi, Modified MAX Phase Synthesis for Environmentally Stable and Highly Conductive Ti_3C_2 MXene, ACS Nano 15 (2021) 6420–6429, https://doi.org/10.1021/acsnano.0c08357.

[35] M. Alhabeb, K. Maleski, B. Anasori, P. Lelyukh, L. Clark, S. Sin, Y. Gogotsi, Guidelines for Synthesis and Processing of Two-Dimensional Titanium Carbide ($Ti_3C_2T_x$ MXene), Chem. Mater 29 (2017) 7633–7644, https://doi.org/10.1021/acs.chemmater.7b02847.

[36] M. Li, J. Lu, K. Luo, Y.B. Li, K.K. Chang, K. Chen, J. Zhou, J. Rosen, L. Hultman, P. Eklund, P.O.Å. Persson, S.Y. Du, Z.F. Chai, Z.R. Huang, Q. Huang, Element Replacement Approach by Reaction with Lewis Acidic Molten Salts to Synthesize Nanolaminated MAX Phases and MXenes, J. Am. Chem. Soc 141 (2019) 4730–4737, https://doi.org/10.1021/jacs.9b00574.

[37] M. Naguib, J. Halim, J. Lu, K.M. Cook, L. Hultman, Y. Gogotsi, M.W. Barsoum, New Two-Dimensional Niobium and Vanadium Carbides as Promising Materials for Li-Ion Batteries, J. Am. Chem. Soc 135 (2013) 15966–15969, https://doi.org/10.1021/ja405735d.

[38] O. Mashtalir, M.R. Lukatskaya, M.Q. Zhao, M.W. Barsoum, Y. Gogotsi, Amine-Assisted Delamination of Nb_2C MXene for Li-Ion Energy Storage Devices, Adv. Mater 27 (2015) 3501–3506, https://doi.org/10.1002/adma.201500604.

[39] J.Y. Tang, X. Huang, T.F. Qiu, X.Y. Peng, T.T. Wu, L. Wang, B. Luo, L.Z. Wang, Interlayer Space Engineering of MXenes for Electrochemical Energy Storage Applications, Chem. Eur. J 27 (2021) 1921–1940, https://doi.org/10.1002/chem.202002283.

[40] J. Yan, C.E. Ren, K. Maleski, C.B. Hatter, B. Anasori, P. Urbankowski, A. Sarycheva, Y. Gogotsi, Flexible MXene/Graphene Films for Ultrafast Supercapacitors with Outstanding Volumetric Capacitance, Adv. Funct. Mater 27 (2017) 1701264, https://doi.org/10.1002/adfm.201701264.

[41] M. R. Lukatskaya, O. Mashtalir, C. E. Ren, Y. Dall'Agnese, P. Rozier, P. L. Taberna, M. Naguib, P. Simon, M. W. Barsoum, Y. Gogotsi, Cation Intercalation and High Volumetric Capacitance of Two-Dimensional Titanium Carbide, Science, 341 (2013), p. 1502, 10.1126/science.12414.

[42] M.R. Lukatskaya, S.M. Bak, X.Q. Yu, X.Q. Yang, M.W. Barsoum, Y. Gogotsi, Probing the Mechanism of High Capacitance in 2D Titanium Carbide Using In Situ X-Ray Absorption Spectroscopy, Adv. Energy Mater 5 (2015) 1500589, https://doi.org/10.1002/aenm.201500589.

[43] J.M. Li, N. Kurra, M. Seredych, X. Meng, H.Z. Wang, Y. Gogotsi, Bipolar carbide-carbon high voltage aqueous lithium-ion capacitors, Nano Energy 56 (2019) 151–159, https://doi.org/10.1016/j.nanoen.2018.11.042.

[44] Y.H. Wang, D.Y. Zhang, Y. Lu, W.X. Wang, T. Peng, Y.G. Zhang, Y. Guo, Y.G. Wang, K.F. Huo, J.K. Kim, Y.S. Luo, Cable-like double-carbon layers for fast ion and electron transport: An example of CNT@NCT@MnO_2 3D nanostructure for high-performance supercapacitors, Carbon 143 (2019) 335–342, https://doi.org/10.1016/j.carbon.2018.11.034.

[45] Y. Li, Y.F. Zheng, L.S. Bao, Hierarchically Structured Porous Materials for Energy Conversion and Storage, Adv. Funct. Mater 22 (2012) 4634–4667, https://doi.org/10.1002/adfm.201200591.

[46] K. Zhu, H.Y. Zhang, K. Ye, W.B. Zhao, J. Yan, K. Cheng, G.L. Wang, B.F. Yang, D. X. Cao, Two-Dimensional Titanium Carbide MXene as a Capacitor-Type Electrode for Rechargeable Aqueous Li-Ion and Na-Ion Capacitor Batteries, ChemElectroChem 4 (2017) 3018–3025, https://doi.org/10.1002/celc.201700523.

[47] K. Zhu, X. Yan, Y.Q. Zhang, Y.H. Wang, A.Y. Su, X.F. Bie, D. Zhang, F. Du, C. Z. Wang, G. Chen, Y.J. Wei, Synthesis of $H_2V_3O_8$/Reduced Graphene Oxide Composite as a Promising Cathode Material for Lithium-Ion Batteries, ChemPlusChem 45 (2014) 447–453, https://doi.org/10.1002/cplu.201300331.

[48] Y. Li, Y. Deng, J. Zhang, Y.e. Han, W. Zhang, X. Yang, X. Zhang, W. Jiang, Tunable energy storage capacity of twodimensional $Ti_3C_2T_x$ modified by a facile two-step pillaring strategy for high performance supercapacitor electrodes, Nanoscale 11 (45) (2019) 21981–21989, https://doi.org/10.1039/C9NR07259D.